AIAA 99-2504

Basic Vorticity Dynamics in a Porous Channel of the Closed-Open Type. Part II:

A Space-Reductive Perturbation Treatment

Joseph Majdalani
Marquette University
Milwaukee, WI 53233

Conference and Exhibit
20–24 June 1999
Los Angeles, CA

Basic Vorticity Dynamics in a Porous Channel of the Closed-Open Type. Part II: A Space-Reductive Perturbation Treatment

J. Majdalani*
Marquette University, Milwaukee, WI 53233
T. S. Roh†
California Institute of Technology, Pasadena, CA 91125

   In extending previous work, this paper continues to address the acoustico-vortical coupling inside a porous channel of the closed-open type. The companion paper (Majdalani, J., "Basic Vorticity Dynamics in a Porous Channel of the Closed-Open Type. Part I: A Standard Perturbation Treatment," AIAA Paper 99-2503) applies conventional perturbation principles to extract the temporal vorticity from the linearized vorticity transport equation. Two alternative efforts will be invested here to extract the temporal velocity from the linearized momentum equation. These efforts rest on applying WKB and multiple-scale expansions. The multiple-scale approach includes the innovative idea of introducing a virtually arbitrary scale that can be left unspecified during the derivation process. At the conclusion of the asymptotic analysis, this unknown variable is determined. The algebraic complexity of the resulting variable (which could not have been guessed beforehand) justifies the 'reverse engineering' methodology adopted in its derivation. Its complexity stems from its intrinsic function of singly representing a triple-deck structure of inner, intermediate, and outer length scales. This spatial scale reduction allows a conventional two-variable multiple-scale expansion to be successful. The emerging one-term formulation is conveniently short and accurate. As a result, closed form expressions for the velocity modulus and depth of penetration can be rendered. Numerical verifications reveal that the error associated with this space-reductive perturbation solution is more accurate than its precursors, namely, the standard perturbation solution of Paper I and the WKB solution furnished here. It is gratifying to note, in closing, that our asymptotic formulas agree very well with computational data acquired from a two-dimensional Navier-Stokes solver that handles the nonlinear mass, energy, and momentum conservation equations.

I.   Introduction

THE purpose of this paper is to complete the temporal flowfield investigation of the porous channel of the closed-open type that was initiated in the companion article (Majdalani, J., "Basic Vorticity Dynamics in a Porous Channel of the Closed-Open Type. Part I: A Standard Perturbation Treatment, AIAA Paper 99-2503, henceforth referred to as Paper I). Previously, it was shown that, in the presence of injection through the porous walls, acoustic pressure waves gave rise, at the solid boundaries, to a strong system of shear waves. These shear waves coupled with the longitudinal acoustic waves to precipitate (fairly) rich flow patterns. The emerging vortical structures were analyzed in Paper I in light of both asymptotic and numeric solutions of the linearized Navier-Stokes equations. To that end, the asymptotic formulations of the temporal field were derived from the vorticity transport equation using a number of successive approximations. In order to reduce the element of uncertainty introduced in the previous derivation, the current investigation will focus on two additional methods, namely, on WKB and multiple-scale expansions. At present, these will be directly applied to the momentum equation. Implementation of these two asymptotic techniques, which is by no means trivial, will lead to alternative expressions that can be used to confirm the solution of Paper I. Thus one of the goals of Paper II will be to provide dual verifications to the former asymptotic analysis. Another goal will be to exploit the benefits of the new formulations. In fact,

---

both WKB and multiple-scale solutions will be shown to provide shorter, more accurate, and more elegant expressions that reveal the explicit relationship between several key parameters. Among them will be the dependence of the penetration depth (of shear waves) on flow variables and acoustic mode numbers.

Analysis of the penetration depth is, of course, equivalent to studying the character of the so-called acoustic boundary layer. This layer is essentially a measure of the rotational region affected by the presence of solid boundaries. In recent years, this acoustic boundary layer has drawn considerable attention in the rocket combustion stability community, due to its role in explaining a number of combustion mechanisms that evolve in the vicinity of the burning surface. In searching for works that address the context of acoustic boundary layers in channels and tubes with both ends closed, one may cite Avalon et al.,[1], Beddini,[2,3] Beddini and Roberts,[4,5] Brown et al.,[6] Casalis et al.,[7] Crump and Price[8] Culick[9-11] Dunlap et al.,[12] Flandro,[13-15] Kirkkopru et al.,[16] Majdalani and Van Moorhem,[17,18] Majdalani[19,20] Roh et al.,[21] Roh and Culick,[22] Vuillot,[23,24] Vuillot and Avalon,[25] and Zhao and Kassoy.[26] Note that these studies consider both laminar and turbulent, reactive and nonreactive, acoustic boundary layers. A contemporaneous investigation introduced by Casalis et al.[7] addresses the channel configuration that we consider here, namely, with the open aft end. As we extend the work of Paper I, we continue to limit our scope to laminar and nonreactive boundary layers.

A third goal of this investigation is to undergo comparisons with numerical predictions acquired from a computational code that solves the nonlinear, Navier-Stokes equations. The undisputed verification that gives our theoretical model a *raison d'être* lies, perhaps, in showing that the asymptotic formulation arrived at after tedious algebra and mathematical maneuvers does indeed agree with the unbiased Navier-Stokes predictions. Only then could we truly justify the linearization procedure that was invoked at the beginning stages set out in Paper I.

With these goals in mind, we start in Sec. II the process of deriving the time-dependent velocity from the linearized Navier-Stokes equations. This is accomplished by applying separation of variables to the linearized momentum equation. At the outset, a singular ODE emerges that requires a careful assessment. Since the solution exhibits an oscillatory behavior, our first attempt will be to invest in a WKB expansion that is ideally suited to extract a one-term expression. Next, a two-variable derivative expansion method is called for.

In principle, the first nonzero term of a multiple-scale expansion is usually more compact and accurate than its counterpart obtained with other asymptotic schemes.

The improved accuracy can be ascribed to multiple-scale formalism which draws information from the first order solution in constructing the leading-order term. In practice, however, the technique can be quite challenging because it presupposes the knowledge of the modified scales associated with the boundary layer structure. As it will be demonstrated below, if (y_0, y_1) represent the base and modified variables, the current problem necessitates the usage of a nonlinear scaling transformation for the modified variable. The nonlinear transformation that must be conjectured in our problem at the beginning of a standard multiple-scale analysis turns out to be

$$y_1 = \varepsilon \left[\sec(\tfrac{\pi}{2} y_0) \tan(\tfrac{\pi}{2} y_0) + \ln \tan \tfrac{\pi}{4}(1 + y_0) \right], \quad (1)$$

which, for obvious reasons, cannot be guessed beforehand. Physically, this difficulty can be attributed to the presence of a triple-deck structure of inner, intermediate and outer spatial scales.[19] The single modified variable y_1 that can be successfully employed in the perturbative analysis must be representative of all three spatial scales. In other words, y_1 must reproduce three spatial scales, thus reducing the total number of virtual scales from three to one. The subsequent two-scale (y_0, y_1) formulation will, in essence, be equivalent to a standard four-scale expansion. Evidently, the two-scale formulation that uses the space-reductive variable y_1 will be more compact and accurate since its leading-order term will be equivalent to a three-term standard multiple-scale expansion. To aggravate the issue, in the case at hand, we do not have the luxury of a choice, since a standard four-scale expansion is futile due to intractable mathematical obstructions. We are bound to pursue, in consequence, the space-reductive treatment.

Since the key scaling transformation y_1 is initially unknown, the asymptotic treatment begins with an undetermined coordinate transformation. At the conclusion of the analysis, this unspecified transformation will be determined from physical arguments. Interestingly, the leading-order WKB expression, that is developed early on, is recoverable from the leading-order space-reductive solution.

Comparisons with the previous solution of Paper I are brought into perspective in Sec. III. Having insured the reliability of the space-reductive formulation, the corresponding modulus and penetration depth are quantified to help characterize the flow behavior in a closed-open configuration. The error entailed in the space-reductive solution is evaluated and compared to its precursor. This is followed by comparisons with computational results retrieved from numerical simulations of the nonlinear Navier-Stokes equations. Section IV concludes the analysis.

II.   Mathematical Procedure

A.   Separation of Variables

In Paper I, the rotational velocity was produced from the vorticity and vorticity transport equations following a number of successive approximations. Here, the temporal component $\tilde{u}$ will be extracted directly and explicitly from the momentum equation, written at $\mathcal{O}(M)$. Using the same notation as before, we rearrange Eq. (26) of Paper I into

$$x \frac{\partial \overline{u}}{\partial x} = \frac{2}{\pi} S \csc(\frac{\pi}{2} y)$$

$$\times \left\{ \left[i - \frac{\pi}{2} \sigma \sin(\frac{\pi}{2} y) \right] \overline{u} - \sigma \cos(\frac{\pi}{2} y) \frac{\partial \overline{u}}{\partial y} + \varepsilon \frac{\partial^2 \overline{u}}{\partial y^2} \right\}. \quad (2)$$

We then call for separation of variables in order to investigate a solution of the type

$$\overline{u}(x, y) = X(x) Y(y). \quad (3)$$

Inserting Eq. (3) back into Eq. (2), and setting $\theta = \frac{\pi}{2} y$ renders,

$$\frac{2S}{\pi Y} \csc(\theta) \left\{ \left[i - \frac{\pi}{2} \sigma \sin(\theta) \right] Y - \sigma \cos(\theta) \frac{dY}{dy} + \varepsilon \frac{d^2 Y}{dy^2} \right\}$$

$$= \frac{x}{X} \frac{dX}{dx} = \lambda_n, \quad (4)$$

where λ_n must be strictly positive for a nontrivial outcome. For every λ_n, a solution X_n and Y_n must be realized. Integration of the axially dependent equation is straightforward. The exact result is $X_n(x) = c_n x^{\lambda_n}$, where c_n is a simple integration constant. Owing to the linearity of Eq. (2), the general solution takes the form

$$\overline{u}(x, y) = \sum_{\lambda_n} c_n x^{\lambda_n} Y_n(y), \quad (5)$$

where Y_n must be determined from the no-slip boundary condition at the wall that is chiefly responsible for the strong coupling between pressure and vorticity modes. As a consequence of this, rotational and irrotational components of the axial velocity must be equal and opposite at the wall. This is fulfilled when, $\tilde{u} = -\hat{u}$, or

$$\overline{u}(x, 0) = -i \sin(k_m x), \quad (6)$$

where $k_m = (m - \frac{1}{2})\pi / l$ is the nondimensional wave number. Inserting Eq. (6) into Eq. (5), writing out the MacLaurin series expansion for the Sine function, and equating summation terms yields

$$\sum_{\lambda_n} c_n x^{\lambda_n} Y_n(0) \equiv -i \sum_{n=0}^{\infty} \frac{(-1)^n (k_m x)^{2n+1}}{(2n+1)!}, \quad (7)$$

which will be true if, for integral values of n,

$$c_n = -i \frac{(-1)^n (k_m)^{2n+1}}{(2n+1)!}, \quad (8)$$

$$Y_n(0) = 1, \quad (9)$$

turning Eq. (5) into

$$\overline{u}(x, y) = -i \sum_{n=0}^{\infty} \frac{(-1)^n (k_m x)^{2n+1}}{(2n+1)!} Y_n(y). \quad (10)$$

Finally, the velocity eigenfunction Y_n is left to be determined from Eq. (4), viz.

$$\varepsilon \frac{d^2 Y_n}{dy^2} - \sigma \cos \theta \frac{dY_n}{dy} + \left[i - \frac{\pi}{2} \sigma(1 + \lambda_n) \sin \theta \right] Y_n = 0$$

$$(11)$$

which must satisfy the two existing boundary conditions:

$$Y_n(0) = 1, \text{ and } \frac{dY_n(1)}{dy} = 0. \quad (12)$$

Unfortunately, Eq. (11) does not possess an exact, closed-form solution. The presence of a small multiplier in the highest derivative suggests, however, the possibility of a perturbation treatment. Due to the oscillatory solution behavior, both WKB and two-variable multiple-scale expansions appear promising. In fact, the latter technique has been shown by Majdalani[19] to result in partially valid local solutions corresponding to outer, inner, and intermediate scales. In the same work, a uniform two-scale expansion was presented using a hybrid technique. The technique was based on the choice of a so-called 'composite scale' that reproduced the inner, outer, and transition scales in their respective domains. Instead of constructing the composite scale from our possible foreknowledge of inner, outer, and transition scales, we now attempt another route to determine the necessary scaling transformation.

B.   The WKB Motivation

In searching for an asymptotic solution to the boundary value problem set out in Eqs. (11)-(12), two cases may arise depending on the order of the Strouhal number.

1.   The Outer Expansion

For small Strouhal numbers, $\sigma = S^{-1} = \mathcal{O}(1)$, and the leading-order term of the outer solution Y_n^o can be obtained straight-forwardly from

$$-\sigma \cos \theta \frac{dY_n^o}{dy} + \left[i - \frac{\pi}{2} \sigma(1 + \lambda_n) \sin \theta \right] Y_n^o = 0. \quad (13)$$

Fulfillment of $Y_n(0) = 1$ gives

$$Y_n^o = [\cos(\frac{\pi}{2} y)]^{\lambda_n + 1} \exp\left\{ \frac{2}{\pi} i S \ln \tan\left[\frac{\pi}{4}(1 + y) \right] \right\}$$

$$\equiv (\cos \theta)^{2n+2} \exp(\frac{2}{\pi} i S \operatorname{gd}^{-1} \theta). \quad (14)$$

where gd^{-1} is the inverse Gudermannian function.[27] Since the cosine factor in Y_n^o decays rapidly as $y \to 1$, the other boundary condition at the core is self-satisfied by the first derivative. This eliminates the need for an inner solution at this order. On a separate note, the exponential term in Y_n^o denotes an oscillatory behavior that is commensurate with the size of S. The first order correction can be found in a similar fashion. The resulting outer solution, at $\mathcal{O}(\varepsilon^2)$, is

$$Y_n^o = (\cos\theta)^{2n+2} \exp(\tfrac{2}{\pi}\mathrm{i}S\mathrm{gd}^{-1}\theta)(1$$

$$-\varepsilon S\{\tfrac{1}{\pi}S^2(\mathrm{gd}^{-1}\theta + \sec\theta\tan\theta) + \pi(n+1)\mathrm{gd}^{-1}\theta$$

$$-\pi(n+1)(2n+\tfrac{1}{2})[\sec\theta\tan\theta + \ln\cos\theta - \ln(1-\sin\theta)]$$

$$+\mathrm{i}S(2n+\tfrac{3}{2})\tan^2\theta\}) . \qquad (15)$$

Due to the $\mathcal{O}(\varepsilon S^3)$ correction term in Eq. (15), a secular behavior can be expected for large S. Since oscillations often occur for $S > 10$, a WKB analysis will be more appropriate in practice.

2. The WKB Expansion

For large Strouhal numbers, $\sigma << 1$, and rapid oscillations occur on a short scale, while a slow drift takes place on the scale $x = \mathcal{O}(1)$. The WKB ansatz can be formulized from

$$-\cos(\tfrac{\pi}{2}y)Y_n' + \mathrm{i}SY_n = 0, \; Y_n(0) = 1,$$

or $\qquad Y_n = \exp(\tfrac{2}{\pi}\mathrm{i}S\mathrm{gd}^{-1}\theta). \qquad (16)$

Setting $Y_n = g(y)\exp(\tfrac{2}{\pi}\mathrm{i}S\mathrm{gd}^{-1}\theta)$ and substituting back into Eq. (11) gives

$$g' + \left[\varepsilon S^3\cos^{-3}\theta + \pi(n+1)\tan\theta\right]g = \mathcal{O}(\varepsilon S^2). \quad (17)$$

The leading-order WKB formulation, at $\mathcal{O}(\varepsilon S^2)$, can be obtained therefrom:

$$Y_n^0 = (\cos\theta)^{2n+2}\exp(\zeta_0 - \mathrm{i}\Phi_0),$$

where

$$\zeta_0 = -\tfrac{1}{\pi}\xi(\mathrm{gd}^{-1}\theta + \sec\theta\tan\theta),$$

$$\Phi_0 = -\tfrac{2}{\pi}S\mathrm{gd}^{-1}\theta . \qquad (18)$$

Here $\xi = \varepsilon S^3 = k^2\nu h v_w^{-3}$ controls the exponential rate of decay as $y \to 1$. The superscript in Y_n^0 refers to the zero order WKB expansion whose derivative automatically satisfies the remaining boundary condition at the core.

C. The Space-Reductive Treatment

Following the approach described by Majdalani,[19] we introduce two independent virtual coordinates, $y_0 = y$, and $y_1 = \varepsilon s(y)$, where 's' is an undetermined scale function that we propose to find. Note that the proposed transformation represents a slight departure from conventional linear transformations bearing $y_1 = \delta(\varepsilon)y$. The current stipulation of y_1 offers the necessary freedom that will lead to a uniformly valid solution.

As prescribed by multiple-scale formalism, functions and derivatives can be expanded, following this virtual transformation, via

$$Y_n(y_0, y_1) = Y_0(y_0, y_1) + \varepsilon Y_1(y_0, y_1) + \mathcal{O}(\varepsilon^2), \quad (19)$$

$$\frac{\mathrm{d}}{\mathrm{d}y} = \frac{\partial}{\partial y_0} + \varepsilon\frac{\mathrm{d}s}{\mathrm{d}y_0}\frac{\partial}{\partial y_1}, \; \frac{\mathrm{d}^2}{\mathrm{d}y^2} = \frac{\partial^2}{\partial y_0^2} + \mathcal{O}(\varepsilon). \quad (20)$$

After substitution into Eq. (11), terms of the same order can be segregated to produce the following set of coupled, partial differential equations

$$\frac{\partial Y_0}{\partial y_0} + \left[\frac{\pi}{2}(1+\lambda_n)\tan(\theta_0) - \mathrm{i}S\sec(\theta_0)\right]Y_0 = 0, \quad (21)$$

$$\frac{\partial Y_1}{\partial y_0} + \left[\frac{\pi}{2}(1+\lambda_n)\tan(\theta_0) - \mathrm{i}S\sec(\theta_0)\right]Y_1$$

$$= -\frac{\mathrm{d}s}{\mathrm{d}y_0}\frac{\partial Y_0}{\partial y_1} + S\sec(\theta_0)\frac{\partial^2 Y_0}{\partial y_0^2}; \qquad (22)$$

where $\theta_0 = \frac{\pi}{2}y_0$. In much the same way, boundary conditions given by Eq. (12) can be converted into

$$Y_0(0) = 1, \; \frac{\partial Y_0}{\partial y_0}(1) = 0 . \qquad (23)$$

Next we integrate Eq. (21) to get

$$Y_0 = C_1\exp\left\{\ln(\cos\theta_0)^{1+\lambda_n} + \frac{2\mathrm{i}}{\pi}S\ln\tan\left[\frac{\pi}{4}(1+y_0)\right]\right\}$$

$$\equiv C_1(y_1)\chi(y_0) , \qquad (24)$$

where C_1 is an integration function that must be determined in a manner to ensure a secular-free series expansion in Y_n. Differentiating Eq. (24), and plugging the results back into Eq. (22) gives

$$\frac{\partial Y_1}{\partial y_0} + \left[\frac{\pi}{2}(1+\lambda_n)\tan\theta_0 - \mathrm{i}S\sec\theta_0\right]Y_1$$

$$= \left\{-\frac{\mathrm{d}s}{\mathrm{d}y_0}\frac{\mathrm{d}C_1(y_1)}{\mathrm{d}y_1} + C_1(y_1)\sec\theta_0\right.$$

$$\times\left[-S^3\sec^2\theta_0 + \frac{\pi^2}{4}(1+\lambda_n)(\lambda_n\tan^2\theta_0 - 1)S\right.$$

$$\left.\left.-\mathrm{i}\pi S^2\left(\frac{1}{2}+\lambda_n\right)\sec\theta_0\tan\theta_0\right]\right\}\chi(y_0), \qquad (25)$$

Removing secular-producing terms demands that the right-hand side of Eq. (25) be *nil*. Otherwise, the asymptotic series will contain terms whose quotient between two successive orders can be unbounded. Fortunately, the resulting first-order differential equation in C_1 can be easily integrated in closed form. After reverting back to our laboratory coordinate, satisfaction of Eq. (23) furnishes

$$C_1(y) = \exp\left\{-\xi\left[\eta(y)\sec^3\theta - \eta(0)\right] + \xi\sigma^2\frac{\pi^2}{4}\right.$$

$$\times(1+\lambda_n)\left[\sec\theta\eta(y)(\lambda_n\tan^2\theta - 1) + \eta(0)\right]$$

$$\left.-\mathrm{i}\pi\xi\sigma\left(\frac{1}{2}+\lambda_n\right)\eta(y)\sec^2\theta\tan\theta\right\}, \qquad (26)$$

where the viscous parameter $\xi = \varepsilon S^3$ appears here along with the effective scale functional $\eta(y)$. The latter is defined by

$$\eta(y) \equiv s(y) / s'(y). \qquad (27)$$

The leading-order term can now be summoned from Eqs. (26) and (24). Since the overall solution is sought at $\mathcal{O}(M)$, and $M > \varepsilon$, there is no justification in retaining other than Y_0, and the expansion in Eq. (20) reduces to

$$Y_n = (\cos\theta)^{1+\lambda_n}\exp\left\{-\xi\left[\eta\sec^3\theta - \eta(0)\right] + \frac{\pi^2}{4S^2}\xi(1+\lambda_n)\right.$$

$$\times\left[\eta\sec\theta(\lambda_n\tan^2\theta - 1) + \eta(0)\right] + \frac{2}{\pi}\mathrm{i}S\mathrm{gd}^{-1}\theta$$

$$\left.-\mathrm{i}\pi\frac{\xi}{S}\left(\frac{1}{2}+\lambda_n\right)\eta\sec^2\theta\tan\theta\right\} + \mathcal{O}(\varepsilon). \qquad (28)$$

Obviously, the undetermined scale function remains, at present, unspecified. However, one can verify that, near the wall, an asymptotic solution exists for $s(y) = y$, as shown in detail by Majdalani.[19] Mathematically, this translates into

$$\lim_{y\to 0}\eta(y) = y \Rightarrow \eta(0) = 0, \qquad (29)$$

which can be used to slightly simplify Eq. (28) before eventual substitution into Eq. (10). Note that this simplification is convenient but not necessary for the success of the current procedure. At the outset, we get

$$\tilde{u}(x,y,t) = -\mathrm{i}\cos\theta\sum_{n=0}^{\infty}\frac{(-1)^n(k_m x\cos\theta)^{2n+1}}{(2n+1)!}$$

$$\times\exp\left\{-\xi\eta\sec^3\theta\left[1 + \frac{\pi^2}{2}\sigma^2(n+1)(\cos 2\theta + 2n\sin^2\theta)\right]\right.$$

$$\left. + \frac{2}{\pi}\mathrm{i}S\ln\tan(\tfrac{\theta}{2}+\tfrac{\pi}{4}) - \mathrm{i}\pi\xi\sigma(2n+\tfrac{3}{2})\eta\sec^2\theta\tan\theta - \mathrm{i}k_m t\right\}$$

$$+ \mathcal{O}(\varepsilon), \qquad (30)$$

which is a rapidly converging series that displays distinctly terms of $\mathcal{O}(\sigma^2)$. In fact, the error associated with $n \geq 1$ terms can be verified to be smaller than the $\mathcal{O}(\varepsilon)$ entailed in the $n = 0$ term.

D. A Finite Formulation

Careful examination of Eq. (30) reveals that a closed-form equivalent is possible when terms that do not affect the reported precision are dropped. This can be accomplished by dismissing the $\mathcal{O}(\sigma^2)$ quantities

arising in the $n \geq 1$ terms. In practice, the equivalent expression reads

$$\tilde{u} = -\mathrm{i}\cos\theta\sin(k_m x\cos\theta)\exp\zeta\exp\left[-\mathrm{i}(k_m t + \Phi)\right] \quad (31)$$

where $$\zeta = \zeta_0 + \zeta_1$$

$$= -\xi\eta\sec^3\theta - \tfrac{\pi^2}{2}\xi\sigma^2\eta\sec^3\theta\cos 2\theta, \qquad (32)$$

and $$\Phi = \Phi_0 + \Phi_1$$

$$= -\tfrac{2}{\pi}S\ln\tan(\tfrac{\theta}{2}+\tfrac{\pi}{4}) + \tfrac{3\pi}{2}\xi\sigma\eta\sec^2\theta\tan\theta \quad (33)$$

Clearly, each of the spatial damping function ζ and spatial phase angle Φ comprises a leading-order term and a small correction of $\mathcal{O}(\sigma^2)$.

E. Remaining Flow Variables

Having obtained an accurate expression for $\tilde{u}$, the transverse component $\tilde{v}$ can be extracted from mass conservation. To that end, we proceed heuristically by setting an *ansatz* of the form

$$\tilde{v} = G(y)\cos(k_m x\cos\theta)\exp\zeta\exp\left[-\mathrm{i}(k_m t + \Phi)\right], \quad (34)$$

where $G(y)$ is a subsidary function that must be determined in a manner to satisfy continuity, namely, $\partial\tilde{u} / \partial x + \partial\tilde{v} / \partial y = 0$. After some algebraic operations, continuity is indeed fulfilled in leading-order quantities when $G = Mv_0^3$. Henceforth,

$$\tilde{v} = M\cos^3\theta\cos(k_m x\cos\theta)\exp\zeta\exp\left[-\mathrm{i}(k_m t + \Phi)\right] \quad (35)$$

indicating that our initial claim of $\tilde{v} / \tilde{u} = \mathcal{O}(M)$ was legitimate. Indubitably, this analytical realization can be verified numerically as well. Next in line, temporal vorticity can be issued directly from the velocity formulation. In fact, differentiation begets

$$\tilde{\omega}(x,y,t) = -S\sin(k_m x v_0)\exp\left[\zeta - \mathrm{i}(k_m t + \Phi)\right]. \quad (36)$$

F. Defining the Space-Reductive Transformation

1. Velocity Consideration

One may proceed by contending that the multiple-scale formula should match, in leading order, the uniformly valid WKB expansion. This can be achieved by suppressing terms of $\mathcal{O}(\sigma^2)$ in Eq. (28) and equating the resulting expression to Eq. (18). At the outset, we find that

$$-\xi\eta\sec^3\theta = -\tfrac{1}{\pi}\xi(\mathrm{gd}^{-1}\theta + \sec\theta\tan\theta),$$

or $$\eta = \tfrac{1}{\pi}(\cos\theta\mathrm{gd}^{-1}\theta + \tan\theta)\cos^2\theta \qquad (37)$$

From Eq. (27), one may solve for the appropriate scale function via $s' - \eta^{-1}s = 0$. Recalling that $s(0) = 0$, direct integration yields

$$s(y) = \exp\int_0^y \eta^{-1}(\tau)\mathrm{d}\tau$$

$$= \sec\left(\tfrac{\pi}{2}y\right)\tan\left(\tfrac{\pi}{2}y\right) + \ln\tan\tfrac{\pi}{4}(1+y) . \qquad (38)$$

With this choice of s, the multiple-scale solution given by Eq. (31) will coincide with the corresponding WKB formulation when $\zeta_1 = \Phi_1 = 0$. Retention of the first order corrections ζ_1 and Φ_1 in Eq. (31) slightly increases the accuracy of the space-reductive multiple-scale formulation beyond its WKB counterpart.

2. Vorticity Consideration

The current expression for vorticity can be compared to its counterpart in Sec. V(F) of Paper I. Knowing that the exponential decay of time-dependent vorticity must be decreed by the same agents irrespective of the perturbation technique, the spatial damping function ζ must be the same as that obtained previously. This contention implies that, in Eq. (32), we must have

$$-\eta \sec^3\left(\tfrac{\pi}{2}y\right) = -\tfrac{1}{\pi}\left[\ln\tan\tfrac{\pi}{4}(1+y) + \sec\left(\tfrac{\pi}{2}y\right)\tan\left(\tfrac{\pi}{2}y\right)\right],$$
$$(39)$$

which leads to the same expressions obtained from velocity consideration.

3. Generalized Space-Reductive Scale

Combining Eqs. (37) and (38), a general expression for the space-reductive function $s(y)$ can be produced:

$$s(y) = \exp \int_0^y \frac{v_0^{-3}(\tau)\mathrm{d}\tau}{\int_0^\tau v_0^{-3}(z)\mathrm{d}z} \qquad (40)$$

since
$$\eta(y) = v_0^{-3}(y)\int_0^y v_0^{-3}(z)\mathrm{d}z \qquad (41)$$

These expressions exemplify the mathematical sophistication materialized in determining explicitly the modified variable transformation. They also indicate that the unusually rapid variations that occur in the transverse direction are solely prescribed by the normal mean flow velocity component, $v_0 = \cos\left(\tfrac{\pi}{2}y\right)$.

4. Comparison with Previous Scaling Analyses

Fortuitously, we are able to manage, this time, an exact expression for the desired nonlinear transformation, $y_1 = \varepsilon s(y)$. Obviously, the complexity of Eq. (38) precludes the possibility of guessing this coordinate transformation beforehand, as demanded by conventional multiple-scale procedures. It also justifies the need to deploy the 'reverse engineering' process in tracking the scales. The most striking result is, perhaps, the excellent agreement between our current didactic formulation and the *ad hoc* formulation obtained by Majdalani[19] using a forward approach. In the previous analysis, a composite scale $s(y) = y(1-y)^{-3y^{3/2}/2}$ was constructed *ab initio* in a manner to reproduce asymptotically the inner, outer, and intermediate scales

cropping up in the problem. As a result, usage of the composite scale reduced the number of spatial scales to two, which was necessary for the success of the multiple-scale expansion. Subsequently, the effective scale functional η was derived and then substituted into the solution. In the current analysis, η is determined first, and it is only at the conclusion of the analysis that one may verify that the space-reductive coordinate does indeed reduce to the proper spatial scales in their regions of applicability. For instance, in the vicinity of the transpiring wall and core, one can recover the scales found by Majdalani.[19] Thus,

$$y_1 = \varepsilon\left[\sec\left(\tfrac{\pi}{2}y\right)\tan\left(\tfrac{\pi}{2}y\right) + \ln\tan\tfrac{\pi}{4}(1+y)\right]$$
$$\rightarrow \{\varepsilon y,\ y \rightarrow 0,\quad \varepsilon(1-y)^{-2},\ y \rightarrow 1\} \qquad (42)$$

III. Discussion

A. The Temporal Velocity Profile

Since $\tilde{v}/\tilde{u} = \mathcal{O}(M)$, $\tilde{u}$ dominates the vortical description, and the total temporal velocity can be contrived by juxtaposition of irrotational and solenoidal fields. The result, from Eq. (31), is

$$u_1(x,y,t) = \mathrm{i}\{\sin(k_m x)\exp(-\mathrm{i}k_m t)$$
$$- \cos\theta\sin(k_m x\cos\theta)\exp\left[\zeta - \mathrm{i}(k_m t + \Phi)\right]\} . \qquad (43)$$

As Euler's notation is no longer needed, the real part of Eq. (43) can be retrieved into

$$u_1(x,y,t) = \overbrace{\sin(k_m x)\sin(k_m t)}^{\text{irrotational part}}$$
$$\underbrace{-\cos\theta\sin(k_m x\cos\theta)\exp\zeta}_{\text{wave amplitude}}\ \overbrace{\underbrace{\sin(k_m t + \Phi)}_{\text{wave propagation}}}^{\text{rotational part}} . \qquad (44)$$

In a sense, Eq. (44) is the culmination of our labors. Clearly, the first term in Eq. (44) abbreviates the pressure-driven, inviscid response, and the second term represents the vorticity-driven, viscous response. As such, it vividly displays the vortical wave characteristics that permit exacting explicit formulations for the vortical depth of penetration, velocity overshoot, and surfaces of constant phase. Unlike theoretical studies that are concerned with infinitely long channels with oscillatory motions induced by pistons at infinity, a dependence on the axial coordinate x is brought about here by the body's finite length. Further examination of Eq. (44) reveals that the vortical amplitude is decreed by two separate terms: an exponentially damped function owing to viscous dissipation, and a space-harmonic function made possible by inclusion of axial mean flow convection of vorticity fluctuations. Whereas both terms depreciate with increasing distance from the wall, the latter varies

sinusoidally in the streamwise direction. Moreover, inspection of the spatial damping function ζ reveals that successive increases in viscosity promote vortical degeneration. This counterintuitive effect stands behind the unusual character of the acoustic boundary layer which clearly defies Prandtl's classic usage of the term.

B.   Comparison with Former Results

A quick comparison is undertaken in Table 1 where numerical simulations of the *linearized* Navier-Stokes equations, described in Paper I, are compared with the asymptotic results obtained at the downstream end from the space-reductive multiple-scale solution, given by Eq. (44), and the perturbation solution of Paper I. The test case covers a typical set of flow parameters. The last two columns give the percentage deviation of the preceding entries relative to the numerical approximations obtained with negligible error. In fact, by observing the results at different tolerances and mesh sizes, the numerically reported data entries seem to be correct to all decimal places quoted. The numerical code was actually tested on similar differential equations that possess exact solutions to insure the accuracy of every decimal point quoted in the table. It is very satisfying to note the agreement, in many cases, to three or more decimal places, between numerics and asymptotics. In view of such small errors, graphs of velocity and vorticity profiles will appear the same to the naked eye. The compact size of Eq. (44) remains, however, the most convenient for programming and analysis.

C.   Velocity Modulus in the Closed-Open Channel

The compact size of Eq. (44) allows extracting the modulus of the axial velocity which can be used to characterize the flow patterns for the first three oscillation modes. These are shown in Fig. 1 below at several select locations for $S = 25(2m-1)$ and $K = 10^6(2m-1)$. Clearly, the modulus is small at the nth acoustic velocity nodes corresponding to $x/l = n/(m-\tfrac{1}{2})$, for integral values of $n < m$. The effect of increasing viscosity can be easily captured in Fig. 2 where the kinematic viscosity is increased by one order of magnitude. The result is a depreciation in the vortical component and a broadening of the acoustic core. These observations are in perfect agreement with the former assessment of vorticity structures in Paper I.

D.   Quantifying the Acoustic Boundary Layer

It should be pointed out that the total flowfield has been divided in Paper I into a steady part and a time-dependent part. Due to linearity, one may envisage the
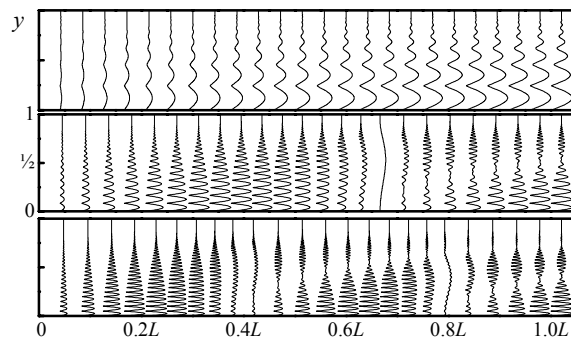
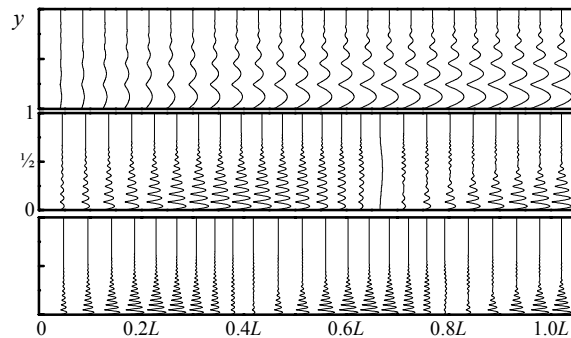**Fig. 1   Modulus of $u^{(1)}$ for $S = 25(2m-1)$, $K = 10^6(2m-1)$, and, from top to bottom, $m = 1, 2, 3$.**

Fig. 2 Same as above except for $K = 10^5(2m-1)$, . This variation can be ascribed to an order of magnitude increase in kinematic viscosity.

Table 1 Temporal velocity $u^{(1)}$ for $S = 25$, $K = 10^5$, $x/l = 1$, $k_m t = \frac{\pi}{2}$, and $m = 1$

y	Numeric	Paper I Asymp.	Paper II Asymp.	Paper I Error %	Paper II Error %
0.00	0.00000	0.00000	0.00000	0.00000	0.00000
0.05	0.68921	0.68928	0.68923	0.00951	0.00176
0.10	1.78448	1.78460	1.78433	0.00682	0.00841
0.15	1.75882	1.75880	1.75907	0.00067	0.01456
0.20	0.66729	0.66709	0.66823	0.02949	0.14208
0.25	0.12864	0.12850	0.12848	0.10981	0.12286
0.30	0.94854	0.94878	0.94639	0.02554	0.22675
0.35	1.76223	1.76254	1.76172	0.01738	0.02890
0.40	1.18939	1.18889	1.19254	0.04168	0.26554
0.45	0.37646	0.37599	0.37720	0.12413	0.19782
0.50	0.93337	0.93462	0.92959	0.13405	0.40470
0.55	1.47594	1.47585	1.47670	0.00616	0.05142
0.60	0.77880	0.77677	0.78143	0.26095	0.33801
0.65	0.90855	0.91150	0.90604	0.32459	0.27688
0.70	1.17433	1.17176	1.17529	0.21877	0.08120
0.75	0.87154	0.87417	0.87167	0.30096	0.01495
0.80	1.04830	1.04377	1.04691	0.43188	0.13277
0.85	1.02134	1.02384	1.02229	0.24420	0.09284
0.90	1.00242	1.00377	1.00326	0.13434	0.08330
0.95	1.00010	1.00000	1.00000	0.01011	0.01004
1.00	1.00000	1.00000	1.00000	0.00000	0.00000

resulting boundary layer as the sum of individual contributions from mean and temporal components.

1. The Mean Flow Contribution

The assessment of the boundary layer associated with the mean flow has been addressed in the past by several researchers including Proudman,[28] Catheral,[29] Cole and Aroesty,[30] and Terrill.[31] For example, Proudman[28] has demonstrated that a shear layer could not exist on a porous surface in the presence of sidewall injection. Accordingly, only suction at the walls can give rise to a shear layer in the vicinity of the solid boundary. This viewpoint is shared by Catheral[29] who explains, in addition, how the conventional viscous shear layer is pushed from the wall, in the injection case, in a manner to delineate two virtually inviscid zones. The first zone consists of the main stream convecting downstream, and the second consists of the incoming stream of injected fluid. This viewpoint is shared by numerous authors, including Cole and Aroesty,[30] in their classic treatment of the 'blowhard' problem over a porous plate.

For an arbitrary cross-flow Reynolds number R, it is therefore quite difficult to locate the viscous shear layer. Fortunately, we know from Terrill[31] that the viscous layer draws nearer to the core with successive increases in R. The thickness of the layer is also confirmed in several investigations to be of $\mathcal{O}(R^{-\frac{1}{2}})$. This implies that the actual steady boundary layer associated with the Taylor flow is vanishingly small. Furthermore, it is pushed all the way to the core, which delimits our solution domain. Evidently, its presence cannot be felt anywhere within the channel, especially near the wall, being a single line that extends along the core. The total boundary layer, if any, must owe its character to the time-dependent contribution.

2. The Temporal Contribution

Contrary to the mean flow, the temporal velocity component gives rise to an appreciable region near the wall where rotational effects are clearly present. This so-called acoustic boundary layer defies Prandtl's classic usage of the term, which is restricted to flows where the dependence on viscosity is consistent with conventional theory. The reason is this. As explained in the preceding section, the rotational region here diminishes when viscosity is increased, a fact that contradicts the traditional expectation of boundary layer growth.

3. The Total Contribution

In quantifying the total boundary layer thickness and location, our task reduces, therefore, to the characterization of the penetration depth y_p of time-dependent rotational waves. We thus define y_p to be the normalized distance from the wall to the point where 99 percent of the rotational wave amplitude in Eq. (44) has vanished. From Eq. (44), one can define the point above the wall where the rotational amplitude reduces to $\alpha = 1$ percent of its irrotational counterpart. If $y = y_p$ denotes such a point, then y_p is soluble from

$$\cos\left(\tfrac{\pi}{2}y_p\right)\sin\left[k_m x\cos\left(\tfrac{\pi}{2}y_p\right)\right]\exp\left[-\eta(y_p)\xi\sec^3\left(\tfrac{\pi}{2}y_p\right)\right]$$
$$-\alpha\left|\sin(k_m x)\right| = 0 . \qquad (45)$$

Despite its transcendental form, Eq. (45) indicates that the exponential decay is a strong function of a nondimensional penetration number, $S_p = \xi^{-1}$. This observation suggests generating curves of y_p versus S_p, for large variations in K and S. In fact, Fig. 3 shows how entire families of asymptotic curves over wide ranges of K and S collapse into single curves per axial position. Here too, asymptotics and numerics concur. This interesting result reveals that y_p does not depend on K and S separately, but rather on $S_p = KS^{-3}$, a parameter that resembles, in importance, the Stokes number in periodic flows over hard walls.[32]

In a sense, Fig. 3 along with Eq. (45) bring into focus the character of the acoustic boundary layer. For instance, it is clear that, for the first oscillation mode, y_p depends on S_p, and, to a much lesser degree, on x. For small S_p, the penetration depth varies linearly with the penetration number, irrespective of x. Apparently, the larger the penetration number, the larger the
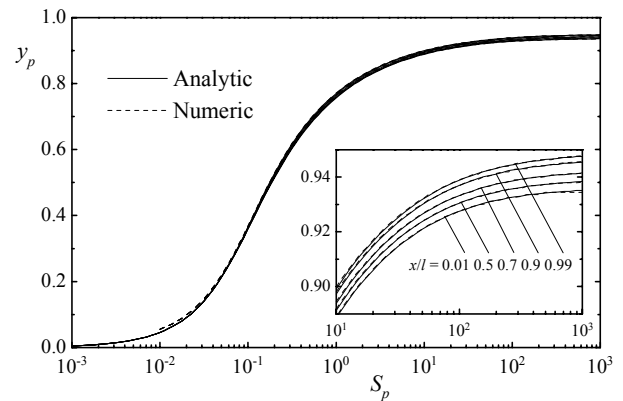
Fig. 3 For the fundamental oscillation mode, we show the acoustic boundary layer thickness over a wide range of parameters and axial stations. We include both numerical ($K = 10^6$) and asymptotic predictions ($10^4 < K < 10^8$). The latter are found to be virtually independent of K. Note the insignificant sensitivity of y_p to the axial location. This effect is captured in the enlarged inset.

penetration depth will be. This dimensionless grouping reveals that increasing injection, or decreasing viscosity, frequency, or channel height broadens the depth of penetration. Notably, our time-dependent solution represents a strongly damped wave whose penetration into the fluid is inversely proportional to ν. The largest possible depth of penetration can be realized, therefore, in a fluid with very small viscosity.

4.   The Maximum Depth of Penetration

   As borne out in Fig. 3, for sufficiently large S_p, y_p approaches a maximum fixed value per axial station. In order to locate this maximum possible depth, $y_{pm} = y_p(\infty, m, x)$, we realize that, for ideal fluids, rotational waves face minimum resistance and extend the furthest from the wall. The asymptotic limit can thus be evaluated from the inviscid formulation of the penetration depth. From Eq. (45), we reap

$$\cos\left(\tfrac{\pi}{2} y_{pm}\right)\sin\left[k_m x \cos\left(\tfrac{\pi}{2} y_{pm}\right)\right] - \alpha \left|\sin(k_m x)\right| = 0 , \quad (46)$$

which possesses an accurate asymptotic expansion with a maximum absolute error of 2.62×10^{-4}, entailed at the smallest value of $y_{pm}(1,0) = 0.9364$. This formula,

$$y_{pm} = 1 - \tfrac{2}{\pi}\sqrt{\alpha \left|\sin(k_m x)\right| k_m^{-1} x^{-1}} + \mathcal{O}\left(1 - y_{pm}\right)^3 , \quad (47)$$

can be used in exchange for the numerical solution of Eq. (46), being correct to $\mathcal{O}(10^{-4})$. Both are shown in Fig. 4 for the first four oscillation modes.

E.   Asymptotic Error Behavior

   To gain further reassurance, we retrace our footsteps from Paper I by analyzing the maximum absolute error between numerics and asymptotics. In much the same way, we again calculate the maximum difference E_m between Eq. (44) and the corresponding numerical solution of the linearized equations. Results are shown in Fig. 5 at several discrete values of the Strouhal number. We also compare our current error to that incurred previously in Paper I. As one can infer from the graph, the order of the error approaches unity very rapidly as $\varepsilon \to 0$. Also, there is a slight improvement in the maximum error associated with the space-reductive multiple-scale formulation.

F.   Comparison with Computational Data

   In order to ascertain the validity of our asymptotics, we insist on comparisons with computational predictions. These are obtained from a dual time-stepping code, developed totally independently by Roh et al.[21] to manage the *nonlinearized* Navier-Stokes equations. The code is devoted to analyzing gas-phase processes based on the complete conservation equations of mass, momentum, and energy. Originally designed to treat propellant combustion in rocket motors, this

implicit dual time-stepping integration method has proven its efficiency and robustness in reacting flows at all speeds. When launched, the algorithm invokes pressure decomposition and preconditioning techniques to circumvent difficulties encountered in low-speed compressible flows. Subsequently, the set of governing equations with appropriate boundary conditions is solved numerically by means of a finite-volume approach. A fully-coupled implicit formulation is then used to enhance numerical stability and efficiency. The scheme has the advantage of achieving a high degree of temporal accuracy with only a modest increase in computational cost. Moreover, since the governing equations are solved implicitly, the numerical method is very stable. As a result, the selection of the integration time step is dictated by the individual process, and not by numerical stability constraints.

   For the same physical parameters employed in our asymptotic formulas, numerical simulations are monitored until convergence is ensured. This is done while keeping the number of binary places as high as possible in order to mitigate the machine's restriction to fixed-point arithmetic. The code relies on a uniform

a)

b)
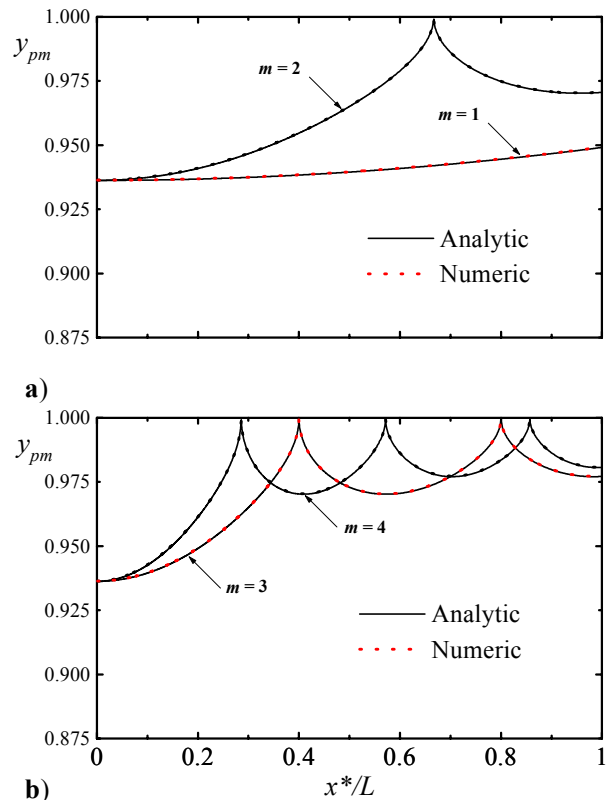
Fig. 4   Trace of the maximum boundary-layer thickness for the first four acoustic modes: a) *m* = 1, 2 and b) *m* = 3, 4. In concurrence with Fig. 3, note the very small axial sensitivity for the first oscillation mode.
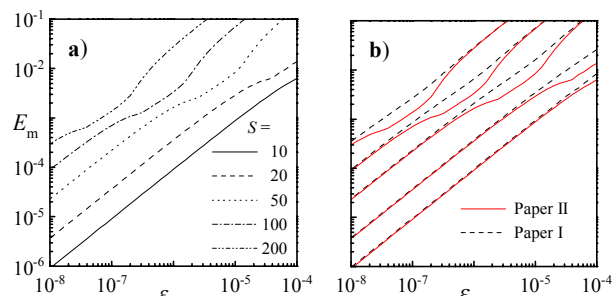
Fig. 5 Maximum absolute error entailed in a) the space-reductive multiple-scale solution of Paper II, and b) both asymptotic solutions of Papers I and II.

mesh resolution and therefore requires more points at higher Strouhal numbers to capture the depreciating vortical waves near the core. We find results obtained for a large number of test cases to be completely satisfactory.

For illustration purposes, we show in Fig. 6 both asymptotics and numerics at three orders of the kinetic Reynolds number. Cases corresponding to $K = 10^7$ and higher become nearly inviscid and bear a striking resemblance to Fig. 6c. In every case, the velocity profiles, characterized by oscillations that progressively decay from the wall, are depicted at two successive times separated by a $\pi / 2$ phase difference. The small disparity between theoretical and computational data can be attributed to small discretization errors and nonlinearity effects that elude our analytic formulation. This agreement is consistent at higher modes where an increasing number of cycles is needed for convergence.

On that account, we show in Fig. 7 both asymptotic and computational predictions for $m = 2$ at the conclusion of several iteration cycles. After fifteen cycles, the discrepancy between theoretical and numerical experiments is hardly visible. In the absence of an exact solution to the case at hand, this comparison to a full Navier-Stokes solution is pivotal. Since the end justifies the means, it gives our approach a *raison d' être* by reconciling between our final analytical formulation and true Navier-Stokes predictions.

IV. Conclusions

In this paper, we have formulated a closed-form asymptotic solution to the two-dimensional time-dependent flowfield established inside a porous channel of the closed-open type. The formulation rested on a space-reductive concept that allowed reducing a triple-deck scaling constitution into one single virtual function. This was an interesting aspect of our theoretical investigation that could possibly be extended to other practical problems. In particular, one may exploit the manner in which the inclusion of an undetermined scale can precipitate the exact
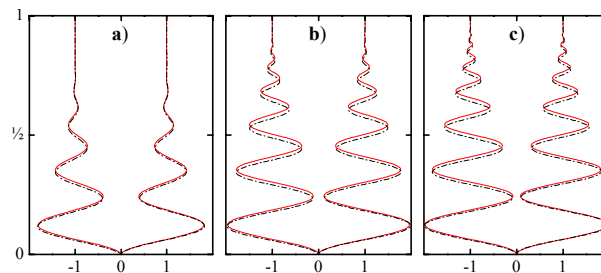
Fig. 6 Comparison between the asymptotic solution (full curves) and numerical simulations of the nonlinear Navier-Stokes equations (chain curves) at two successive times. Here $S = 25$, $x / l = 1$, and $m = 1$. Using a 40x300 mesh resolution, simulation results are shown after 9 iteration cycles for a) $K = 10^4$, b) $K = 10^5$, and c) $K = 10^6$.
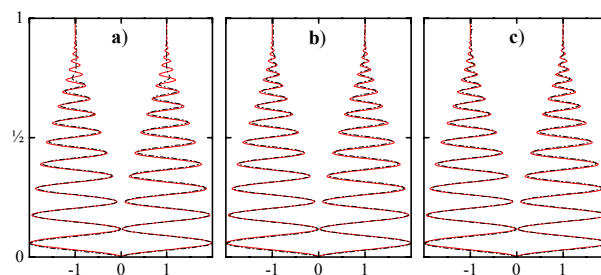
Fig. 7 Comparison between the asymptotic solution (full curves) and numerical simulations of the nonlinearized Navier-Stokes equations (chain curves) at two successive times. Here $K = 2 \times 10^6$, $S = 50$, $x / l = 1 / 3$, and $m = 2$. Using a 40x300 mesh resolution, simulation results are shown after a) 9, b) 12, and c) 15 iteration cycles.

specification of the variable transformation needed for a uniformly valid solution.

The flowfield description emerging from the space-reductive two-scale technique carries numerous advantages: 1) It provides an alternative formulation that can be used to verify the asymptotic solution of Paper I. 2) It reduces to the WKB expansion when its leading-order arguments are solely retained. 3) It provides an explicit expression for the velocity modulus, which helps explain the ensuing flowfield patterns. 4) It provides the means to quantify the acoustic boundary layer. The latter is found to strongly depend on the same dynamic similarity parameter appearing in the closed-closed configuration. 5) Its error exhibits a clear asymptotic behavior that provides the formal mathematical evidence of its validity. 6) It compares well with numerical simulations of both linearized and nonlinear Navier-Stokes solutions. In a sense, we are happy that our analysis could be brought to fruition despite numerous technical challenges.